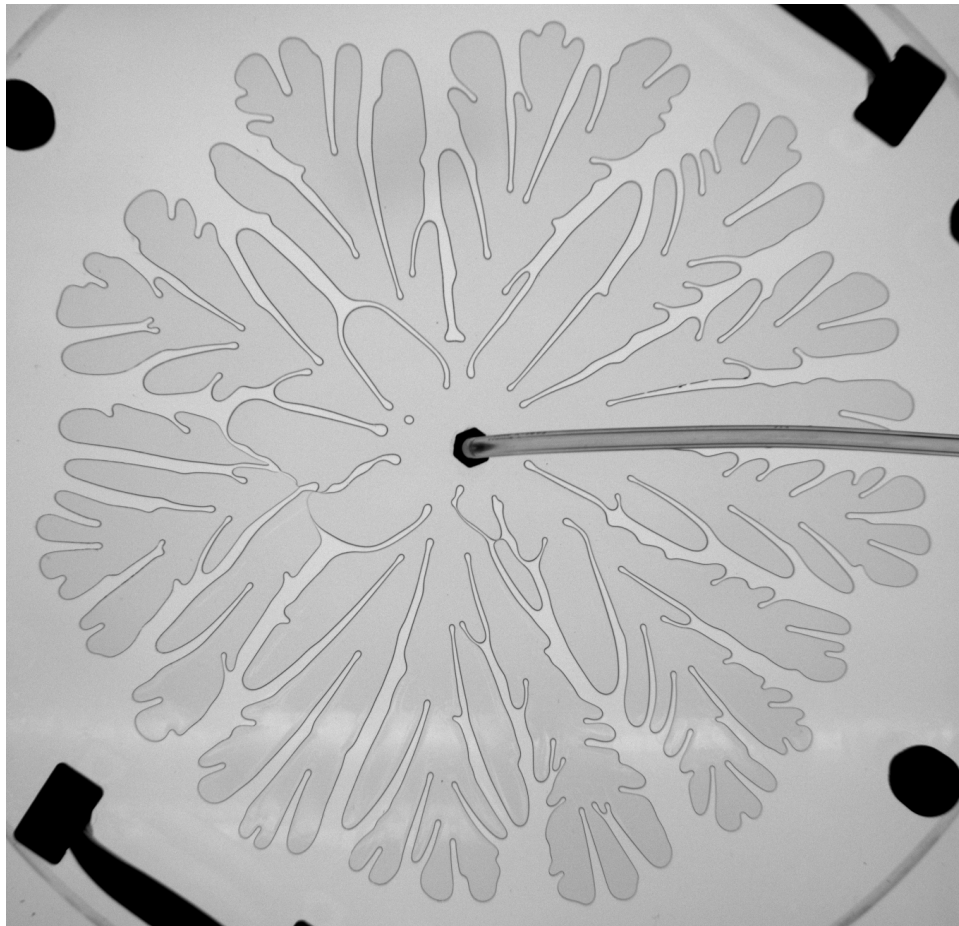


University of Toronto
ADVANCED PHYSICS LABORATORY

FVF

Fractal Viscous Fingering



Revisions

October 29, 2018: [Stephen Morris <smorris@physics.utoronto.ca>](mailto:smorris@physics.utoronto.ca)

Please send any corrections, comments, or suggestions to the professor currently supervising this experiment, the author of the most recent revision above, or the Advanced Physics Lab Coordinator.

[This pdf file has live links that look like this.](#)

Copyright 2017 University of Toronto
This work is licensed under the Creative Commons
Attribution-NonCommercial-ShareAlike 4.0 Unported License.
(<http://creativecommons.org/licenses/by-nc-sa/4.0/>)

1 Introduction

The equations governing the flow of fluids are highly nonlinear [1], which means they are full of surprises. This reflects the very rich phenomenology of fluid motion. Even in simple cases, the equations tend to have many solutions. It is not even known if non-singular solutions always exist, and even when they do, which motion is actually observed depends crucially on the *stability* of the solutions. Boundary conditions are of paramount importance. In this experiment, we will study a situation in which a rather simple, highly viscous flow, a limit for which the motion is governed by linear equations, nevertheless becomes unstable due to the boundary conditions at a *moving* boundary. This instability is of a general class called a *Laplace instability*. The resulting complex pattern is a paradigm case of a very common type of fractal growth which includes the dendritic growth of crystals (like snowflakes), diffusion limited aggregation (DLA), dielectric breakdown, electrodeposition, the branching of propagating cracks and the growth of bacterial colonies, among many others [2, 3]. In this experiment, both the initial linear instability and the emergence of the fractal pattern will be studied.

2 Theory

2.1 general ideas

When a viscous liquid (mineral oil in this experiment) is confined between closely spaced plates, an arrangement known as a *Hele-Shaw cell*, it forms an effectively two dimensional arena for fluid dynamics. The no-slip boundary conditions on the plates enhance the effect of viscosity, putting the flow into the low Reynolds number, *Stokes flow* regime, where viscosity dominates over inertia [1]. The fluid is incompressible, so that

$$\nabla \cdot \vec{\mathbf{u}} = 0 . \quad (1)$$

In this limit, the flow obeys the (linear) Stokes equation,

$$\nabla p = \mu \nabla^2 \vec{\mathbf{u}} , \quad (2)$$

where $\vec{\mathbf{u}}$ is the velocity, p is the pressure and μ is the molecular viscosity of the fluid. Combining these by taking the divergence of Eqn. 2, we arrive at a Laplace equation for the pressure:

$$\nabla^2 p = 0 . \quad (3)$$

As shown in Fig. 1, in the thin direction of the cell, $\vec{\mathbf{u}}(z)$ forms a parabolic profile and its z -averaged velocity in the xy plane of the cell is given by [2]

$$\langle \vec{\mathbf{u}} \rangle = -\frac{b^2}{12\mu} \nabla p , \quad (4)$$

where b is the thickness of the small gap between the plates. This is a version of *D'Arcy's Law*, which governs slow flows inside porous media. Indeed, the instability we are going to study is often used as a 2D model for a similar 3D instability that limits the recovery of oil from porous rock.

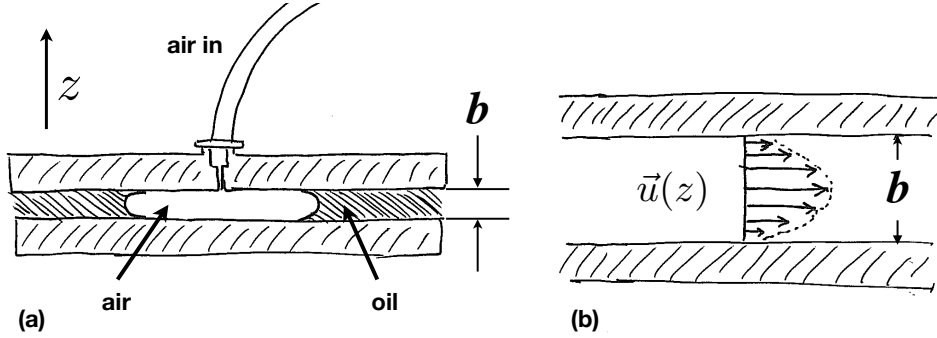


Figure 1: The Hele-Shaw cell. (a) Side view. (b) The parabolic flow profile in the oil.

Now consider injecting a second, different fluid into the space between the plates, displacing the first one. This new fluid is immiscible in the first fluid. In this experiment, the first fluid is mineral oil and the second, injected fluid is compressed air. We can assume that intruding air has a negligible density and viscosity compared to the more viscous oil. At the moving boundary between the second fluid and the first, we have the following kinematic boundary condition:

$$v = \hat{\mathbf{n}} \cdot \langle \vec{\mathbf{u}} \rangle \sim \hat{\mathbf{n}} \cdot \nabla p, \quad (5)$$

where v is the speed of the fluid-fluid boundary motion and $\hat{\mathbf{n}}$ is a unit normal pointing into the more viscous liquid. This condition simply requires that the interface move at the same speed as the liquid does there (hence the name “kinematic”). It amounts to a boundary condition on the gradient of the pressure in the oil. Another pressure boundary condition is related to the surface tension at the liquid-liquid interface. The pressure across a curved interface jumps by an amount proportional to the curvature

$$\Delta p = \gamma \kappa, \quad (6)$$

where γ is the surface tension and κ is the geometric curvature of the interface. The curvature κ is just the inverse of the radius of the “osculating” (kissing) circle tangent to the interface at that point. The sign of κ is such that the pressure is larger in the fluid when the centre of curvature of the interface is inside that fluid. So, for example, the air in a circular bubble surrounded by oil is at a higher pressure than the adjacent oil by an amount proportional to the inverse radius of the bubble.

You might think that injecting air into an oil-filled Hele-Shaw cell would produce a simple circular expanding bubble. It does, but only at first. In fact, the growing bubble soon becomes unstable and develops a complex multi-armed shape. The bifurcating arms are called “fingers”. Curiously, if the more viscous oil is injected into an air filled Hele-Shaw cell, a stable circular “bubble” of oil *does* form. The instability only happens for a lower viscosity fluid injected into a higher one.

The expanding air bubble is unstable due to the *Laplace instability* shown schematically in Fig 2. Any tiny protuberance of a flat interface concentrates ∇p at its tip, which causes the protuberance to extend faster, due to a larger $v = \langle \vec{\mathbf{u}} \rangle \propto -\nabla p$ and the kinematic boundary condition, Eqn. 5. When the injected fluid is air, which has a negligible density and viscosity, then the pressure inside the air is simply constant. The gradient of the pressure ∇p in the oil is then steepest at the tips of protuberances, so they grow faster than the surroundings. The relationship between $\langle \vec{\mathbf{u}} \rangle$ and p is in fact the same as the relationship between the electric field $\vec{\mathbf{E}}$ and the electric potential ϕ , so the fast growth near the tips of protuberances is analogous to the formation of large electric fields near the tips of pointed conductors, like lightning rods. The only thing that prevents the protuberance from

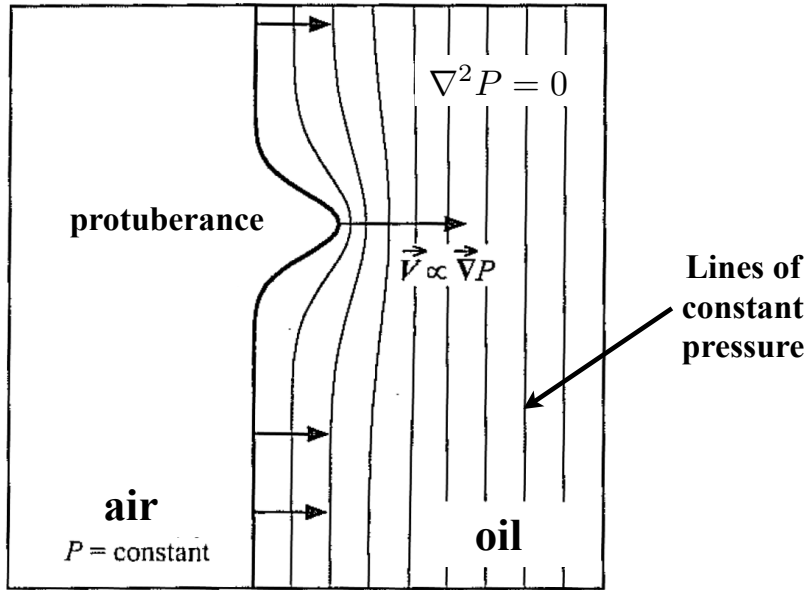


Figure 2: The Laplace instability. Any protuberance creates a pressure gradient that causes its tip to grow faster than the surrounding flat interface. The opposing effect of surface tension is not shown. Adapted from Couder [2].

becoming infinitely sharp is the surface tension boundary condition, Eqn. 6, which tends to *reduce* the pressure gradient ∇p near the tip, tending to smooth out the protuberance. Surface tension is a larger effect for large curvatures (small radii of curvature — sharp tips). Thus, the fingering instability sets in when the competition between these two effects favours growth of tips on some sufficiently large length scale. Thus, an expanding bubble becomes unstable to fingers when it is large enough.

2.2 linear stability analysis

A common way to approach instabilities is to use a form of perturbation theory called *linear stability analysis*. We start by solving the problem for a simple *base state* — a flat moving front or an expanding circular bubble. Then we consider the fate of spatially periodic perturbations of this state. We take the amplitude ξ of the perturbations to be small and linearize the problem to lowest order in the amplitude. The amplitudes are taken to be proportional to growing exponentials: $\xi \sim e^{\sigma t}$. The growth rate σ is then the solution of a solvable linear problem. If $\sigma > 0$ for some periodicity of the perturbation, then the system is unstable for that period, while if $\sigma < 0$, it is stable. The situation of $\sigma = 0$ is *marginally stable*. The periods with the largest growth rates σ may be expected to dominate the periodicity of the initial pattern of fingers, as long as the nonlinearities remain reasonably small. Often multiple modes near the fastest growing ones have positive growth rates, and exactly which modes grow may evolve with time during the linear growth regime. This will turn out to be the case for the present problem.

Linear stability theory is inherently limited however. As soon as the amplitude of the instability has grown significantly, the modes begin to interact and violate the linearizing assumptions of the theory. At that point, linear theory breaks down and a nonlinear theory is required. Going beyond linear theory is typically impossible analytically, and one must resort to numerical simulation, although a few general techniques do exist [4].

Linear stability analyses of the viscous fingering problem go back nearly 60 years, and details are still actively being worked on today. A linear stability theory for a moving, flat interface in was first given by Chuoke [5] and at almost the same time by Saffman and Taylor [6]. Since the latter were more famous, the whole instability is often called the *Saffman Taylor problem*. For an expanding circular bubble, which is the case for our experiment, the linear stability analysis was first carried out by Paterson [7]. In Appendix C, we solve the linear stability problem for flat interfaces and for circular expanding bubbles for a simple 2D fluid model. Then we review some of the more recent developments, and outline a more complete model that we can use to interpret data.

The key results may be summarized as follows;

- The stability of a circular bubble of radius R expanding at radial speed v depends on two dimensionless numbers; the ratio R/b , where b is the gap spacing of the plates and the *capillary number* $Ca = \mu v / \gamma$, where μ is the molecular viscosity and γ is the surface tension.
- As the bubble radius grows, it passes through a sequence of radii $(R/b)_{n_o}$, with $n_o = 2, 3, 4, \dots$, such that it becomes unstable to larger and larger numbers of fingers (*i.e.* more and more values of n acquire positive growth rates σ_n). For $(R/b)_{n_o} < (R/b) < (R/b)_{n_o+1}$, the bubble is unstable to $n = 2, 3, 4 \dots n_o$ fingers.
- To predict the number of fingers we should see at the end of the linear growth regime, we must calculate the accumulated growth of all the possible modes n , and choose the “winner”. A simple and traditional approach is to calculate the fastest growing mode at the initial radius R_0 and velocity v_0 , on the assumption that this mode will have a head start and grow for the longest time. This is clearly inadequate if the initial radius is very small, since many new modes will enter the race as the bubble grows. With both R and v time dependent, it is more reasonable to calculate the accumulated growth of each n as an integral of over the time dependent growth rate σ_n .
- The simplest linear stability theory is only valid in the limit of small Ca (*i.e.* slowly expanding bubbles), so we must use a more general model for $Ca \sim O(1)$. For larger Ca , surface tension effects become progressively less important and the number of fingers is thought to only depend on the ratio R/b , independent of Ca . Linear stability in this limit is not very well understood.

Details are given in Appendix C.2, where a python code that carries out a time integration of the predicted finger growth, `linear_theory.py`, is described. The result is a sort of spectrum of the predicted relative amplitudes of the fingers with various n .

To study the linear regime experimentally, one must grow unstable circular bubbles under various conditions, use image analysis to extract their outlines for the early stages of growth and use these to measure their mean radii and radial growth speed as a function of time. Then, by choosing an appropriate time to mark the end of the linear regime, one can compare the number of (small) fingers observed in the images at that time with the number predicted by linear theory.

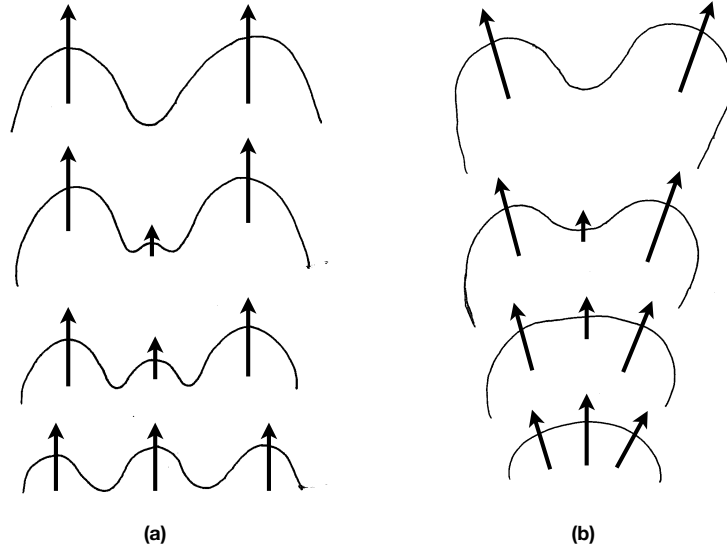


Figure 3: Features of the nonlinear regime. Time progresses upward. (a) Shadowing: one finger is crowded out, so three fingers become two. (b) Tip splitting: one finger broadens and splits into two.

2.3 nonlinear theory

There is not much that analytic theory can do in the strongly nonlinear regime. Detailed simulations [8] are useful, but tend to lack explanatory value. They merely reproduce experiments without really explaining them in a satisfying way. Interest in highly nonlinear pattern-forming systems tends to be focussed on universal features which are found across many diverse systems [9, 10, 11]. Radial viscous fingering serves as a paradigm experimental example of a nonlinear Laplace instability.

2.3.1 general features of the nonlinear regime

When the fingers have grown to a sufficiently large amplitude, they begin a complex nonlinear interaction. All radially growing Laplace unstable systems show a number of generic features that emerge from this interaction. Two phenomena, which are in some sense opposites, are often observed: *shadowing* and *tip splitting*. Shadowing (also sometimes called *shielding*) occurs when three growing fingers compete with each other. If the centre finger falls a bit behind the others, it will tend to lose driving forces and stop growing. The outside fingers crowd it out and “put it in the shade”. Often these small fingers will even retract, due to surface tension, while the larger ones carry on. Shadowing has a tendency to *decrease* the number of viable growing fingers in the early stages of the nonlinear regime. Fig. 3(a) shows the effect. Shadowing is commonly observed in all Laplace unstable systems because growth is always fastest at the farther reaching tips, and these consume all the driving forces.

Tip-splitting tends to generate new fingers from mature existing ones, and thus *increases* the number of fingers. Fig. 3(b) shows this effect. Once a finger has survived shadowing and advanced radially, it tends to develop a broad, growing tip. This tip region is susceptible to the same sort of instability as the original growing circular bubble was. Broad tips bifurcate into two fingers, which then continue outward and eventually compete with each other. Often one of such a pair will later shadow the

other. The result is a complex bifurcating pattern in which a few large fingers develop many side branches from successive splitting and shadowing events. A highly developed fingering pattern may be described as a fractal. Many branching systems [3] exhibit these two characteristic, universal features.

2.3.2 fractal aspects

Fractals are self-similar geometric objects. A physical object may reasonably be described as a random fractal if it is *statistically* self-similar over some suitably wide range of length scales. The highly ramified bubbles produced by the outworking on the nonlinear interactions of the Laplace instability are statistically self-similar in this sense. Many processes that produce highly branched structures may be described as random fractals. Classifying diverse fractal objects or processes is a way of establishing their universal features.

Paterson [9] pointed out that radial viscous fingering, in a certain limit, could be mapped onto diffusion-limited aggregation (DLA), a paradigm model of a process that produces fractal objects. DLA has an enormous literature [10]. In the DLA model, a particle is allowed to make a random walk until it encounters a fixed “seed”. At that point, it sticks to the seed and forms a cluster. A new diffusing particle is then randomly released outside the cluster until it sticks, and the process is repeated until the cluster becomes a large ramified object. The growth of a DLA cluster exhibits a type of Laplace instability, but with none of the smoothing effect of the surface tension that is present in radial viscous fingering. The connection between the two becomes complete only in the limit of small λ_{\max} , the length scale of the fingering instability. Experiments done in this limit [11] show the striking similarity of form with DLA.

The main defining characteristic of random fractal objects is that their forms can be understood in a scale-free manner by certain power-law relationships. The highly ramified bubbles cover a roughly circular region, but do not fill it completely the way a “solid” 2D bubble would. They may be said to have a dimension which is greater than one (a non-area-filling line) and less than two (an area-filling circle). A non-integer *fractal dimension* D is a way of making this idea precise. Known variously as the [Hausdorff](#), [Minkowski-Bouligand](#), or simply the box-counting dimension, it is the exponent in the power law that emerges from the scaling relationship between the number $N(\epsilon)$ of boxes of size ϵ that are required to cover the object and the box size ϵ . Typically the largest box is a single one that covers the whole image, while the smallest is a single pixel. We find

$$N(\epsilon) \sim \epsilon^{-D} \quad \rightarrow \quad D = -\frac{\log N(\epsilon)}{\log \epsilon} . \quad (7)$$

For an ordinary 2D space-filling object, like a circle, this definition recovers the usual dimension $D = 2$. For many ideal, mathematical fractals, a non-integer value of D can be calculated exactly. The [Sierpinski triangle](#), for example, has a dimension of $D = \log 3 / \log 2 \approx 1.58496$. Planar DLA clusters, which must be generated numerically, have a dimension $D \approx 1.71$. You can experiment with making DLA clusters using the python code `DLA.py`, supplied on [the experiment web page](#). The code `box_count.py` implements the box-counting algorithm, plots the power-law and fits it to calculate D .

Another way to arrive at a fractal dimension D is to measure the radius of gyration R_g of the object as its area grows. If I is the moment of inertia, M is the total mass, and m is the mass of a pixel located at radius r_i and $M = mA$, where A is the number of pixels in the cross-sectional area, then

$$I = \sum_i m r_i^2 = M R_g^2 \quad R_g^2 = \frac{1}{A} \sum_i r_i^2 . \quad (8)$$

It can be shown [10, 12] that for a growing fractal object with dimension $D < 2$, the area increases more slowly than R_g^2 , such that

$$A \sim R_g^D \quad R_g \sim A^{1/D} \quad \log R_g = \frac{1}{D} \log A + \text{const.} \quad (9)$$

Thus, D can be found by determining the slope of a log-log plot of R_g vs. A . Ideally, this dimension will agree with the one arrived at by box counting.

In the experiment, we will generate highly nonlinear bubbles and measure their fractal dimensions D and examine how this dimension emerges as the bubble develops.

3 Experiment

3.1 overview

The parameters that may be varied in the experiment are the pressure of the injected air p_g and the spacing between the plates b . The pressure is set by the regulator on the air tank and measured by the large gauge in pounds per square inch (psi). The pressure indirectly controls the speed v of the bubble inflation, which will be measured later from images. The plate spacing is set by six plastic spacers that are clamped in place with brass finger nuts.

Fluid properties are given in Appendix A. Spacer dimensions are given in Appendix B.

3.2 important safety notices

- **This experiment uses compressed air. Make sure you understand the safe handling of the air cylinder and pressure regulator. Always unscrew the red regulator knob all the way and open the vent toggle valve before opening the main supply valve on the top of the tank. Close the main supply valve when leaving the experiment unattended. See Fig. 4 and Section 3.4.3 below.**
- **This experiment uses mineral oil. Oil spilled on the floor may cause a slip hazard. Promptly clean up all small spills with the paper towels provided. Discard oily paper towels in the container provided.**

3.3 general remarks

- **This experiment can be messy!** While the mineral oil is safe to handle, you may wish to wear old clothes or cover your good clothes with a lab coat. You can use latex gloves, if you like. Wipe your hands before touching the computer.
- The oil should rise a few mm above the gap between the plates, but not more than this.

- When an oily hose is not in use, clamp it to the elevated support with the big paper clips provided. Wipe up oil drops on top of the circular plate as these will cause distortions in the images.
- Keep the lid on the tank when not in use to prevent contamination.
- Spacers can be gently washed with water and soap and dried completely before using again. Spacers can also just be wiped and left on a few paper towels to soak up the oil and then used without being washed.
- If the oil is really dirty, it can be changed by draining it into the waste bottle by opening the tank valve, followed by refilling. The brass finger nuts can be removed to allow the plate to gently rest on the tops of the screws temporarily, while oil is draining. Lift the plate by the handles with no hoses attached. Draining the oil may be extremely slow. **Do not do this unless the oil is really dirty.**
- Thorough cleaning requires the drained plate to be washed with plenty of water and dish soap in the sink (a task not to be undertaken lightly). The empty tank itself can be washed with water and dish soap, draining the oil/water/soap mixture into the waste container. Take care that the waste container does not overflow! The tank and plate must be completely dry and free of soap and water before any new oil is added. **Be very careful not to scratch the tank or the plate.** Put something soft in the bottom of the sink before standing the plate in the sink for washing. Only wash with soft sponges. **Do not wash the experiment unless it is absolutely necessary.**

3.4 suggested procedure

3.4.1 initial set up of the Hele-Shaw cell

To set the cell spacing b , loosen the brass finger nuts and lift the plate by the handles. This will be easier with no hoses attached. The six plastic spacers should be positioned just outside each screw, to minimize blockage of the flow. The brass finger nuts should have a soft plastic washer between them and the circular plate. Do not over-tighten! Make sure that all six spacers are matched in thickness before tightening the finger nuts. Spacer dimensions are given in Appendix B.

The oil between the plates should be clean and free of all small bubbles. Even very tiny bubbles (which might be hiding under the brass inlet fitting) will strongly effect the fingers as they grow. Use the peristaltic pump, described below, to clear the cell.

The air inlet pipe should be stretched straight and clamped to the back of the Hele-Shaw tank so that it is in the three o'clock position, as viewed by the camera. This positioning is important for later masking it out of the images.

3.4.2 setting up the camera and lighting

The DC voltage applied to the LED light should be fixed at 40V. The camera is controlled by the FlyCapture2 program. Adjust the focus of the camera with a bubble in the cell by zooming up the image on the screen to see individual pixels. Leave the focus and aperture settings fixed for the experiment. Take a calibration image of the cell with all pipes removed by including a plastic ruler laid on top of the circular plate.

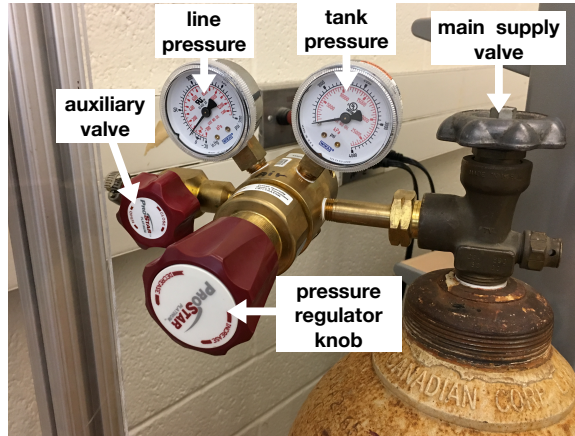


Figure 4: Parts of the air pressure regulator system.

You can use all the default settings of the FlyCapture2 program except the frame rate. In the `camera control` dialog window, uncheck the `auto` box on the frame rate. The frame rate can be set to a precise number by typing in the box. The maximum is 120 fps. The maximum will be needed for the fastest bubbles.

When you press record, you will get the `record settings` window. Here you should set the directory and file name for the run. It is a good idea to use a name that contains information not already recorded by the camera, such as the pressure, the setting of the needle valve, the frame rate, and the plate separation, as indicated by the letter of the spacer. Something like `25psi_needle_open_120fps_D`. The program will add a date and time stamp and a frame number. Use a new directory for each run.

`Saving options` should be set to capture a few hundred frames; a few seconds worth is usually enough. `Image format` should be set to TIFF, with `compression method` set to LZW.

Click the `Start Recording` button *just after* you open the inlet toggle valve.

3.4.3 recording the growth and fingering of a bubble

A run of the experiment consists of quickly opening the inlet toggle valve to apply air pressure to the inlet pipe while simultaneously recording a burst of images with the camera. You can make growing bubbles either from a “standing start” by suddenly opening the valve with no bubble between the plates, or you can prepare a small stationary circular bubble by slightly cracking open the inlet toggle valve before later suddenly applying the full pressure. An initial bubble creates a slightly “cleaner” (*i.e.* better defined) initial condition for the growth of the instability.

You may wish to try pressures that are too small to easily read with the large gauge. You can also use the needle valve (see below) to reach lower flow rates. The highest pressures (about 50 psi) are only needed for the thinnest spacers.

A run is over when the bubble reaches the edge of the circular plate and air begins to leak out. The inlet toggle valve can be closed once this happens.

To set up the air pressure system (see Fig. 4):

- Unscrew the red pressure regulator knob all the way before opening the main supply valve on the top of the air tank. This prevents accidentally supplying too high a pressure to the gauge.
- Make sure the inlet toggle valve is closed and the vent toggle valve is open. The auxiliary valve should be wide open.
- Open main supply valve. The small gauge on the regulator will show the pressure in the tank.
- Screw the red pressure regulator knob in and out until the desired pressure is reached on the large gauge. You will hear air escaping the vent.
- Close the vent toggle valve. The pressure will pop up slightly.
- Now you may either completely open the needle valve (it takes several turns to do this), in which case the inflation rate is controlled by the pressure you have selected on the regulator. Or you may open the needle valve just slightly, in which case the flow will be restricted, leading to slower bubble inflation.
- If you wish to make an initial static bubble, open the inlet toggle valve very slightly to slowly inflate a small circular bubble.
- When the air pressure system is set up and you are ready to shoot, quickly open the inlet toggle valve and click the mouse to trigger the camera. The pressure on the large gauge will drop back down to what you set before.

3.4.4 resetting the Hele-Shaw cell after making a bubble

To reset the Hele-Shaw cell for another shot, do the following:

- Disconnect the air inlet pipe and attach the pipe leading to the inlet of the peristaltic pump (it should be clipped to the vertical support when not in use, to avoid oil dripping).
- Run the peristaltic pump **near its slowest rate** to suck oil and air out from the centre of the circular plate. (Pumping too hard may cause the pipe to come loose, spilling oil.) The output of the pump can be returned to a corner of the Hele-Shaw tank.
- Keep pumping until all the air and small bubbles have been removed. This can take a while.

Vigorous pumping with the peristaltic pump can cause the Hele-Shaw plates to bow together. When the oil-filled pipe is removed, the un-bowing of the plates will suck air into the cell. To avoid this, pump slowly and wait a few minutes after turning off the peristaltic pump before disconnecting the pipe.

3.4.5 shutting down the experiment

When you are finished with the apparatus, do the following:

- Turn off the light and disconnect the pipes to the Hele-Shaw cell. Elevate the inlet and outlet of the peristaltic pump by clipping them to the vertical support.
- Leave the Hele-Shaw cell full of oil to avoid bubbles getting stuck. Wipe up all stray droplets of oil and throw out all oily paper towels.
- Put the lid on the Hele-Shaw cell.
- Shut the main supply valve on the top of the air tank.
- Clear all your images and code off the computer when you are completely done with them. Otherwise, put them in a directory with your name on it.

Remember that the experiment may be used by someone else during the week.

4 data analysis tools

In the experiment the data are mostly in the form of *images*. An image is a 2D position measurement. **Every pixel is a measured data point.** We will be using 8 bit binarized images — images for which every pixel is either black (greyscale level 0) or white (greyscale level 255). All images must be in a format that preserves pixel-level information with lossless compression. Tagged Image Files (.tif) format with LZW compression achieves this. The camera should be set to save images in this format. *Do not use .jpg images except to be used qualitatively as frames in movies.* By default, the python image library (PIL) saves images in uncompressed .tif format, which is fine.

To analyze images, we will use a combination of python codes and an open source application called **Image J**. It is easy to take an overwhelming number of images in this experiment. Storage capacity may become a limitation. Be judicious about choosing frame rates, deleting useless images, decimating the data *etc.* to avoid having more images than can be reasonably analyzed. It's a good idea to do some preliminary runs and then try the analysis on a few images first before taking any detailed data. Image analysis may require long computation times.

Read the comments in the python codes for details about how they work. Only a rough outline is given here. Of course you can modify any of the analysis codes as you see fit. The following are merely suggestions.

4.1 probing the linear instability

To study the linear instability, it is necessary to examine the shape of the growing bubble at early times, as a function of pressure p_g and plate separation b . Low pressures and large plate separations may be easier to study, as fewer fingers are produced.

4.1.1 data analysis workflow for the linear regime

- Use **Image J** and the image of the hole in brass inlet fitting in your calibration image to locate the x, y coordinates of the centre of the cell in pixels. Measure the number of pixels in a long interval of the image of the plastic ruler and use that to convert pixels to length units. Also estimate the width of the inlet pipe and the radius of the inlet fitting in pixels.
- Use the code `process_FVF_images.py` to crop and binarize the images with `empty_pipe = True`. Estimate an outer crop radius in pixels that cuts off most of the long fingers of the nonlinear regime. The code will make a new directory with the processed images. If you have selected the threshold values well, the processed images contain only clear black outlines of the bubble and the initial stages of finger growth. You can decimate the number of images analyzed to reduce the effective frame rate (but keep track of this number, if you do this). Try just a few images first.
- Use the code `mean_radius_FVF.py` to find the mean radius and its statistics. The code reads all the images in the directory made by `process_FVF_images.py`. This will make a plot of the radii vs. frame number and store the data in a text file.
- Scrutinize the images and the plot of the radii to estimate the frame number when the linear regime ends. **Count the fingers in that frame.** The fingers need to be large enough to count reasonably unambiguously, but not so big that they exhibit shadowing or tip splitting. These measurements will be somewhat uncertain, due to the ill defined nature of the duration of the linear regime and what counts as a finger. Some fingers may be obscured by the inlet pipe. Experiment with different criteria and estimate the error in the counted number of fingers. It is probably a good idea to average the number of fingers over several runs with the same parameters.
- Use the code `linear_theory_FVF.py` to analyze the data stored in the text file by `mean_radius_FVF.py`. You will need all the calibration data to convert pixels to length and frame rates to time (accounting for any decimation). You will also have to specify the frames to be included in the linear regime.

The code uses a polynomial fit to the radius and the derivative of this fit to get the varying value of v , and hence Ca . It then calculates the predicted number of fingers in two ways. First, by calculating n_{\max} from Eqn. 63, using initial data R_0/b and Ca_0 , and then by carrying out the full time integration of Eqn. 66. The peak of the resulting growth curve is the predicted number of fingers. Its width gives some measure of the uncertainty in the prediction.

4.2 characterizing the strongly nonlinear pattern

To measure the statistical fractal aspects of the finger patterns, it is necessary to produce binarized and *flood-filled* bubble images. That is, images in which the interior of the bubble is black and the exterior white — with a minimum of stray white or black pixels in each region. The part of the bubble obscured by the inlet pipe has to be dealt with. [An example of a binarized flood-filled image is shown on the experiment web page.](#)

4.2.1 data analysis workflow for the nonlinear regime

- Use **Image J** to determine an outer crop radius which is large enough to enclose the fully developed bubble, but excludes the handles *etc.* Choose the width of the inlet pipe and the radius of the inlet fitting in pixels and determine the x, y coordinates of the centre of the inlet, as above. Discard images where the outermost fingers are cut off by the cropping.
- Use the code `process_FVF_images.py` to crop and binarize the images with `empty_pipe = False` and one or more of the other options for dealing with the inlet pipe, either `reflect_pipe` or `rorschach`, set to `True`. You can also use `empty_pipe = True` and set `edge_pipe = True`. The result will be directories containing the binarized images with various methods for excluding or filling in the inlet pipe region.

The idea of these techniques is to fill the inlet pipe region with something that is at least statistically similar to the rest of the bubble (or not).

- Use the **Image J** tool to manually flood-fill the interior of the bubble in the binarized images. For this to work, there must be no gaps in the outline of the bubble. Gaps can be filled by using tools from the *Image J Process* → *Binary* menu. The function *Dilate* is especially useful for closing gaps in the outline. See [the manual pages](#) for the *Binary* menu for details. You can also just edit the images manually by using the *Paintbrush* tool to colour pixels directly. **Image J** has a useful *Edit* → *Undo* feature for when an attempt to flood-fill goes awry.
- Once the images are properly binarized and flood-filled, their fractal dimensions can be found using the code `box_count.py`. You can also use the **Image J** function *Analyze* → *Tools* → *Fractal Box Count* to do almost exactly the same thing. Several fractal images are posted on [the experiment web page](#) that you can test these algorithms on.
- You can also, in principle, determine the fractal dimension D from the area evolution of the radius of gyration of the flood-filled pattern, as discussed in Sec. 2.3.2 above.

5 questions

The following are some rough ideas for things to study.

5.1 linear regime

- How does the initial capillary number Ca_0 of the expanding bubble, which is proportional to its initial velocity v_0 , vary with the experimental parameters, the pressure p_g and/or plate separation b ? Does it depend on the presence of an initial bubble and its dimensionless radius R_0/b ?
- How consistent is the counted number of fingers at the end of the linear regime from shot to shot, under nominally identical initial conditions?
- How does the counted number of fingers at the end of the linear regime depend on the pressure p_g and plate separation b ? How does it depend on Ca_0 and/or R_0/b ? Plot the counted number of fingers against Ca_0 and/or R_0/b , with other things held constant.

- How well does linear stability theory predict the number of fingers? How does the prediction made using only the initial radius R_0 and velocity v_0 (and hence Ca_0 and R_0/b) compare to the prediction using the full time integration of the growth *via* Eqn. 66? Plot the counted number of fingers against the number predicted by various versions of linear theory.
- How strongly does the agreement or disagreement with linear theory depend on the time you choose to call the end of the linear regime?
- Are there regimes of dimensionless parameters for which linear theory is more or less successful at predicting the number of fingers? Are there systematic trends in the degree of agreement or disagreement with linear theory?
- In the analysis, it is possible to “turn off” the wetting and/or viscous normal stress terms in the expression for the growth rate Eqn. 63. What is the contribution of these effects to the agreement or disagreement between the predicted number of fingers and the number found in the experiment?
- All of the analysis assumed that the flow is in the low Reynolds number, Stokes limit. Is this a good assumption? The Reynolds number, $Re = bv/\nu = b\rho v/\mu$ is actually proportional to the capillary number, with $Re = (b\rho\gamma/\mu^2)Ca \approx 1Ca$, so large Re also corresponds to large Ca .

5.2 nonlinear patterns

- How does the box-counting dimension D of radial viscous fingering compare to DLA or other fractal patterns?
- How does D emerge as the pattern grows in size? Does it approach a clear limit?
- Does D vary under different ways of choosing the boxes? How does the quality of the linear log-log fit whose slope is D depend on parameters? The latter is a measure of how “good” a fractal (close to self-similar) the pattern is.
- Do all fully developed patterns have the same dimension D ? How does it depend on the pressure p_g or plate spacing b ?
- How does the box-counting dimension D compare to the dimension D found from the scaling of the area with the radius of gyration?
- Tip splitting and shadowing are in competition in setting the number of fingers. Which one wins? Find all the local finger tips (suitably defined) and measure their radial positions. Plot a histogram of the number of local finger tips as a function of their radii. How does this histogram evolve as the pattern grows?

References

(Electronic versions, if available, are accessible by clicking on the title.)

- [1] D. J. Acheson, *Elementary Fluid Dynamics*, Oxford University Press (1990).
- [2] Y. Couder, *Perspectives in Fluid Dynamics*, Cambridge University Press (2003), page 53; [[link to pdf](#)]
- [3] P. Ball, *Nature's Patterns: a Tapestry in Three Parts*, Oxford University Press (2009), part 3, *Branches*.
- [4] J. A. Miranda and M. Widom, *Radial fingering in a Hele Shaw cell: a weakly nonlinear analysis*, Physica D., **120**, 315 (1998).
- [5] R. L. Chuoke, P. van Meurs, & C. van der Poel, *The instability of slow, immiscible, viscous liquid-liquid displacements in permeable media*, Petroleum Trans. AIME **216**, 188 (1959).
- [6] P. Saffman & G. I. Taylor, *The penetration of a fluid into a porous medium or Hele-Shaw cell containing a more viscous liquid*. Proc. R. Soc. Lond. **A 245**, 312 (1958).
- [7] L. Paterson, *Radial fingering in a Hele Shaw cell*, J. Fluid Mech., **113**, 513 (1981).
- [8] A. Segall, O. Vantzios and M. Ben-Chen, *Hele-Shaw Flow Simulation with Interactive Control using Complex Barycentric Coordinates*, Proceedings of ACM Symposium on Computer Animation, Zurich, 2016.
- [9] L. Paterson, *Diffusion-limited aggregation and two-fluid displacements in porous media*, Phys. Rev. Lett., **52**, 1621 (1984).
- [10] T. Viscek, *Fractal growth phenomena*, World Scientific (1992).
- [11] O. Praud and H. L. Swinney, *Fractal dimension and unscreened angles measured for radial viscous fingering*, Phys. Rev. E., **72**, 011406 (2005).
- [12] S. E. May and J. V. Maher, *Fractal dimension of radial fingering patterns*, Phys. Rev. A, **40**, 1723 (1989).
- [13] G. M. Homsy, *Viscous fingering in porous media*, Ann. Rev. Fluid Mech., **19**, 271 (1987).
- [14] S. S. S. Cardoso and A. W. Woods, *The formation of drops through viscous instability*, J. Fluid Mech., **289**, 351 (1995).
- [15] Paterson actually treated the case when the input volumetric flow rate $Q = dV/dt = b(dA/dt) = 2\pi bR(dR/dt)$ is constant, where V is the volume and A is the area of the bubble. In this case, the radial speed of expansion of the bubble is *not* constant. It turns out that v also varies for our constant pressure experiment. Such time dependence makes no difference for Stokes flows, because Eqn. 2 has no time derivative.
- [16] C. Park and G. M. Homsy, *Two-phase displacement in Hele-Shaw cells: Theory*, J. Fluid Mech., **139**, 291(1984).
- [17] E. O. Dias and J. A. Miranda, *Wavelength selection in Hele-Shaw flows: a maximum amplitude criterion*, Phys. Rev. E., **88**, 013016 (2013).

- [18] T. Maxworthy, *Experimental study of interface instability in a Hele-Shaw cell*, Phys. Rev. A, **39**, 5863 (1989).
- [19] M. Nagel and F. Gallaire, *A new prediction of wavelength selection in radial viscous fingering involving normal and tangential stresses*, Phys. Fluids, **25**, 124107 (2013).
- [20] H. Kim, T. Funada, D. D. Joseph and G. M. Homsy *Viscous potential flow analysis of radial fingering in a Hele-Shaw cell*, Phys. Fluids, **21**, 074106 (2009). This paper is followed by a remarkable appendix added by an unidentified non-author, who was allowed by the editor to comment on its significance. He calls the paper “a totally new approach” and “a bold step”. The fact that this term was overlooked for 50 years might be partly because it is small in the flat interface case and only becomes crucial in the radial version of the experiment. But it is an interesting illustration of the fact that in fluid mechanics, getting the boundary conditions right is the really hard part, not solving the equations.
- [21] D. A. Reinelt, *Interface conditions for two-phase displacement in Hele-Shaw cells*, J. Fluid Mech., **183**, 219 (1987). In fact, the thickness of the wetting layers leads to a small correction to the kinematic condition at the interface (Eqn. 6a in Reinelt). This effect is ignored even in the “full” theory of Dias *et al* [17].

property	symbol	value	units	temperature
surface tension	γ	$(3.3 \pm 0.1) \times 10^{-2}$	N/m	
density	ρ	$(0.860 \pm 0.001) \times 10^3$	kg/m ³	
molecular viscosity	μ	0.180 ± 0.002	kg/(m s)	20°C
		0.155 ± 0.002		22.5°C
		0.135 ± 0.002		25°C

Table 1: Properties of the mineral oil.

spacer letter	colour	thickness (mm)
A	orange	0.791 ± 0.004
B	transparent	1.051 ± 0.003
C	transparent	1.303 ± 0.003
D	transparent	1.512 ± 0.003
E	white	2.334 ± 0.003
F	white	3.206 ± 0.005

Table 2: Thicknesses of the spacers.

A fluid properties

Table 1 shows the properties of the mineral oil used. The mineral oil is “heavy industrial grade”, supplied by [McMaster-Carr](#). Other oily liquids with different properties could also be used (*e.g.* baby oil, cooking oil). It is important that the fluid wet the plastic plates completely; oils and other non-polar hydrocarbons do this, but water does not. See the python code `viscosity_vs.T.py` for a function that accounts for the temperature dependence of μ . The *capillary number* is given by $Ca = \mu v / \gamma$. The *kinematic viscosity*, which is needed to calculate the Reynolds number $Re = bv / \nu$, is defined to be $\nu = \mu / \rho$.

B spacer dimensions

Table 2 shows the dimensions of the spacers. With some care, spacers can be stacked to make larger thicknesses.

C linear stability theory

We begin our outline of linear stability theory in Sec. C.1 with the classic case of the stability of a moving flat interface, and then in Sec. C.2, we generalize this result to an expanding circular bubble. We employ a simplified 2D model of the Hele-Shaw flow in which the pressure jump boundary condition is simply proportional to the curvature of the interface in the plane of the cell, as in Eqn. 6. After decades of very detailed work [13, 16, 17, 18], including important experiments by Maxworthy [18], it has been shown that this simple boundary condition fails to account for some additional 3D and viscous effects, which have been incorporated more recently by (among others) Dias *et al* [17]. In Sec. C.3, we outline these effects and present (without detailed derivation) the result for the linear growth rate in a full theory that includes them. In Sec. C.4, we tie up a few loose ends and in Sec. C.5, we describe a practical way to apply the full linear stability theory to experimental observations.

It is fair to say that work on this problem is still ongoing with agreement with experiment still somewhat lacking, even at the level of linear stability. Some recent papers suggest going beyond the D’Arcy approximation [19].

C.1 linear stability of a 2D, moving flat interface

The derivation here is adapted from Couder [2]. We consider a 2D fluid in the xy plane with an initially flat interface located at $x = vt$. The air bubble occupies $x < vt$, while the oil fills $x > vt$. Since the air is assumed to have zero density and zero viscosity, it is just at constant pressure $p = p_a$. The oil is moving uniformly toward $+x$ at constant speed $v = \langle \vec{u} \rangle$. The pressure in the oil for the flat interface can be found by integrating Eqn. 4

$$v = \langle \vec{u} \rangle = -\frac{b^2}{12\mu} \left(\frac{dp}{dx} \right) \quad \rightarrow \quad v(x - x_0) = -\frac{b^2}{12\mu} (p - p_0) , \quad (10)$$

where we take $x_0 = vt$ and $p_0 = p_a$. Since the interface is flat, Eqn 6 implies $\Delta p = p(x_0) - p_a = 0$. This solves for the pressure in the oil for what is known as the *base state* (superscript (0)):

$$p(x, t) = p^{(0)}(x, t) = p_a - \frac{12\mu}{b^2} v(x - vt) . \quad (11)$$

Now consider a small perturbation of the position of the interface from $x = vt$ to

$$x = \xi(x, y, t) = vt + \hat{\xi} e^{\sigma t} e^{iky} , \quad (12)$$

where $\hat{\xi}$ is the (formally infinitesimal) amplitude and σ the growth rate of the perturbation, which is sinusoidal in the y direction with wavenumber k . Our objective is to find $\sigma(k)$. Next, we expand the pressure in the oil as follows

$$p = p^{(0)} + p^{(1)} = p^{(0)} + \hat{p}(x) e^{\sigma t} e^{iky} . \quad (13)$$

This has to be a solution of the Laplace equation, Eqn. 3, in the oil and in particular we know that $p^{(1)}$ must die away to zero as $x \rightarrow +\infty$. We know from general principles that solutions of the Laplace equation do this exponentially with the wavelength of the disturbance on the boundary, so we put $\hat{p}(x) \sim e^{-k(x-vt)}$ so that

$$p^{(1)} = \tilde{p} e^{-k(x-vt)} e^{\sigma t} e^{iky} , \quad (14)$$

where \tilde{p} is another infinitesimal amplitude. You can check that this is indeed a solution of the Laplace equation. Next, using Eqn. 5, we match the x component of the velocity

$$\langle \vec{\mathbf{u}} \rangle_x = \langle \vec{\mathbf{u}} \rangle_x^{(0)} + \langle \vec{\mathbf{u}} \rangle_x^{(1)} = \frac{\partial \xi}{\partial t} = v + \hat{\xi} \sigma e^{\sigma t} e^{iky} . \quad (15)$$

Now we can use Eqn. 4 at the interface $x = \xi$ to find the relationship between the amplitudes

$$-\frac{b^2}{12\mu} \frac{\partial}{\partial x} \left(p^{(0)} + p^{(1)} \right) \Big|_{x=\xi} = \langle \vec{\mathbf{u}} \rangle_x^{(0)} + \langle \vec{\mathbf{u}} \rangle_x^{(1)} \quad (16)$$

$$\tilde{p} \left(\frac{b^2 k}{12\mu} \right) e^{-k(x-vt)} e^{\sigma t} e^{iky} \Big|_{x=\xi} = \hat{\xi} \sigma e^{\sigma t} e^{iky} , \quad (17)$$

$$\tilde{p} = 12 \left(\frac{\mu \sigma}{b^2 k} \right) \hat{\xi} \quad (18)$$

where we can safely take $x = \xi = vt$, to lowest order, in the exponential. From this we conclude the perturbed pressure in the oil is

$$p^{(1)} = 12 \left(\frac{\mu \sigma}{b^2 k} \right) \hat{\xi} e^{-k(x-vt)} e^{\sigma t} e^{iky} . \quad (19)$$

Now we need to impose the surface tension boundary condition Eqn. 6 with

$$\kappa = \frac{\partial^2 \xi}{\partial y^2} , \quad (20)$$

for our simplified 2D model. Higher order terms in the curvature may be neglected. Applying Eqn. 6 gives

$$\Delta p|_{x=\xi} = \left[p - p_a \right]_{x=\xi} = \left[p^{(0)} + p^{(1)} - p_a \right]_{x=\xi} = \gamma \frac{\partial^2 \xi}{\partial y^2} \quad (21)$$

$$\left[p_a - \left(\frac{12\mu}{b^2} \right) v(x - vt) + \left(\frac{12\mu\sigma}{b^2 k} \right) \hat{\xi} e^{-k(x-vt)} e^{\sigma t} e^{iky} - p_a \right]_{x=\xi} = \quad (22)$$

$$- \left(\frac{12\mu}{b^2} \right) v(vt + \hat{\xi} e^{\sigma t} e^{iky} - vt) + \left(\frac{12\mu\sigma}{b^2 k} \right) \hat{\xi} e^0 e^{\sigma t} e^{iky} = \quad (23)$$

$$= \gamma \frac{\partial^2}{\partial y^2} \left(vt + \hat{\xi} e^{\sigma t} e^{iky} \right) = -\gamma k^2 \hat{\xi} e^{\sigma t} e^{iky} \quad (24)$$

$$- \left(\frac{12\mu v}{b^2} \right) + \left(\frac{12\mu\sigma}{b^2 k} \right) = -\gamma k^2 , \quad (25)$$

again using $x = \xi = vt$ in the exponential. From this we finally get the so-called *dispersion relation*

$$\sigma(k) = vk - \frac{\gamma b^2}{12\mu} k^3 , \quad (26)$$

which is plotted in Fig. 5. Let us think carefully about what this result means. Whenever $\sigma(k) > 0$ for some k , the interface is unstable to fingering at that wavenumber. The plot shows that the interface is always unstable for a range of k between zero and k_o , for all positive v . The case of negative v , which describes a front of oil moving into an air-filled gap, is always stable with $\sigma(k) < 0$ for all k .

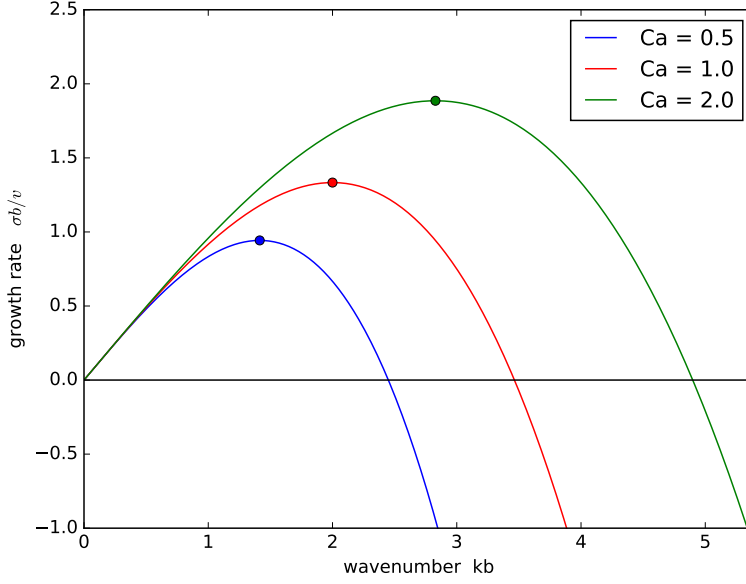


Figure 5: The dimensionless dispersion relation $\sigma b/v$ vs. kb , for various values of $Ca = \mu v/\gamma$. Ca is effectively the dimensionless interface velocity. The solid points show the maximum growth rates $k_{\max}b$. Adapted from Couder [2].

The wavenumber of maximum growth rate k_{\max} is the peak of $\sigma(k)$, where

$$\left. \frac{d\sigma}{dk} \right|_{k=k_{\max}} = 0 \quad \rightarrow \quad k_{\max} = \frac{2}{b} \sqrt{\frac{\mu v}{\gamma}}. \quad (27)$$

The growth rate at k_{\max} is given by

$$\sigma_{\max} = \sigma(k_{\max}) = \frac{2v}{b} \sqrt{\frac{\mu v}{\gamma}} - \frac{2\gamma}{3b} \left(\frac{\mu v}{\gamma} \right)^{3/2}. \quad (28)$$

It turns out that the largest unstable wavenumber $k_o = \sqrt{3} k_{\max}$. The corresponding wavelength of maximum growth rate is $\lambda_{\max} = 2\pi/k_{\max}$ is

$$\lambda_{\max} = \pi b \sqrt{\frac{\gamma}{\mu v}}. \quad (29)$$

In dimensionless terms

$$\left(\frac{\lambda}{b} \right)_{\max} = \pi Ca^{-1/2} \quad \text{where} \quad Ca = \frac{\mu v}{\gamma} \quad (30)$$

is the dimensionless *capillary number*. In dimensionless form, the dispersion curve is

$$(\sigma b/v) = (kb) - \frac{1}{12 Ca} (kb)^3. \quad (31)$$

This is what is actually plotted in Fig. 5 for various values of $Ca \sim v$. The dimensionless maximum growth rate is simply

$$(\sigma b/v)_{\max} = \frac{4}{3} Ca^{1/2}. \quad (32)$$

Thus, linear theory predicts that fingers will grow from infinitesimal perturbations (any tiny noise is enough), and grow fastest with a spacing of λ_{\max} . But there exists a certain range of wavelengths around λ_{\max} that also have significant positive growth rates. There exists a small length scale $\lambda_o = 2\pi/k_o$ below which all perturbations are smoothed out by surface tension. This is the main result of the calculation.

We now generalize this result to a circular expanding bubble.

C.2 linear stability of a 2D expanding circular bubble

The linear stability of an expanding circular bubble was first examined by Paterson [7]. Our treatment of this case is adapted from Refs. [7, 4, 14]. We consider an expanding circular air bubble of radius $R(t) = vt$ [15]. Inside the bubble, for $r < R$, the pressure is constant at p_a . In the oil outside, for $r > R$ the pressure is $p(r)$. Following similar steps as in the previous section, we first find the pressure $p^{(0)}(r)$ in the base state.

In circular coordinates, the Laplace equation for $p(r)$ is

$$\nabla^2 p = \frac{1}{r} \frac{d}{dr} \left(r \frac{dp}{dr} \right) = 0, \quad (33)$$

which can be immediately integrated twice to give

$$r \frac{dp}{dr} = A \quad \frac{dp}{dr} = \frac{A}{r} \quad p(r) = A \log r + B, \quad (34)$$

with A, B constants. At $r = R$, we have

$$p(R) = A \log R + B = p_a - \frac{\gamma}{R}, \quad (35)$$

where the last term is the contribution of surface tension. Take a moment to think carefully about the sign of this term. Subtracting Eqn. 34 from Eqn. 35, we eliminate B to get

$$p(r) = A \log \left(\frac{r}{R} \right) + p_a - \frac{\gamma}{R}. \quad (36)$$

We can find A using Eqn. 4,

$$\langle \vec{u} \rangle = -\frac{b^2}{12\mu} \left(\frac{dp}{dr} \right) = -\frac{b^2}{12\mu} \left(\frac{A}{r} \right) \quad (37)$$

$$v = \langle \vec{u} \rangle|_{r=R} = -\frac{b^2}{12\mu R} A \quad (38)$$

$$A = -12 \left(\frac{\mu v R}{b^2} \right). \quad (39)$$

So the base state pressure in the oil is

$$p^{(0)} = p_a - \frac{\gamma}{R} - 12 \left(\frac{\mu v R}{b^2} \right) \log \left(\frac{r}{R} \right). \quad (40)$$

Now we are ready to perturb the position of the interface from $r = R = vt$ to $r = \xi$, with

$$\xi = vt + \hat{\xi} e^{\sigma t} e^{in\theta}, \quad (41)$$

with $\hat{\xi}$ an infinitesimal amplitude and $n = 2, 3, 4, \dots$. Now the perturbation is “quantized” because the circumference of the bubble has a finite length and only an integer number of infinitesimal fingers will fit around it. $n = 1$ is omitted because $\xi \sim e^{i\theta}$ just shifts the circular bubble off centre, so it does not grow in volume.

Next we write the pressure perturbation as

$$p(r) = p^{(0)} + p^{(1)} = p^{(0)} + \hat{p} e^{\sigma t} e^{in\theta} . \quad (42)$$

As before, we need the infinitesimal amplitude $\hat{p}(r)$ to die away as $r \rightarrow +\infty$, and for $p^{(1)}$ to obey the Laplace equation. This can be accomplished by choosing $\hat{p} = \tilde{p}(r/R)^{-n}$. The Laplace equation becomes

$$\nabla^2 p^{(1)} = \left(\frac{1}{r} \left(r \frac{\partial}{\partial r} \right) + \frac{1}{r^2} \frac{\partial^2}{\partial \theta^2} \right) \left[\tilde{p} \left(\frac{r}{R} \right)^{-n} e^{\sigma t} e^{in\theta} \right] = 0 . \quad (43)$$

You can confirm that this is indeed the case. Next we invoke the boundary condition Eqn. 5 at the bubble surface to match the radial velocity

$$\langle \vec{\mathbf{u}} \rangle_r = \langle \vec{\mathbf{u}} \rangle_r^{(0)} + \langle \vec{\mathbf{u}} \rangle_r^{(1)} = \frac{\partial \xi}{\partial t} = v + \hat{\xi} \sigma e^{\sigma t} e^{in\theta} \quad (44)$$

Now we can use Eqn. 4 at the interface $r = \xi$ to find the relationship between the amplitudes

$$-\frac{b^2}{12\mu} \frac{\partial}{\partial r} \left(p^{(0)} + p^{(1)} \right) \Big|_{r=\xi} = \langle \vec{\mathbf{u}} \rangle_r^{(0)} + \langle \vec{\mathbf{u}} \rangle_r^{(1)} \quad (45)$$

$$\left[v - \hat{\xi} \left(\frac{v}{R} \right) e^{\sigma t} e^{in\theta} - \left(\frac{b^2}{12\mu} \right) \tilde{p} (-n) r^{-n-1} R^n e^{\sigma t} e^{in\theta} \right]_{r=\xi} = v + \hat{\xi} \sigma e^{\sigma t} e^{in\theta} , \quad (46)$$

$$\tilde{p} = 12 \left(\frac{\mu R}{nb^2} \right) \left(\sigma + \frac{v}{R} \right) \hat{\xi} , \quad (47)$$

where we have used $r = \xi = R$, to lowest order. We finally get

$$p^{(1)} = 12 \left[\frac{\mu R}{nb^2} \right] \left(\sigma + \frac{v}{R} \right) \hat{\xi} e^{\sigma t} \left(\frac{R}{r} \right)^n e^{in\theta} . \quad (48)$$

We can now apply the surface tension boundary condition Eqn. 6. The full expression for the in-plane curvature κ is somewhat [more complex in 2D polar coordinates](#):

$$\kappa = - \frac{\xi^2 + 2 \left(\frac{\partial \xi}{\partial \theta} \right)^2 - \xi \left(\frac{\partial^2 \xi}{\partial \theta^2} \right)}{\left(\xi^2 + \left(\frac{\partial \xi}{\partial \theta} \right)^2 \right)^{3/2}} . \quad (49)$$

The negative sign in front is there to ensure that our sign convention has $\kappa = -1/R$ for a circular bubble. Putting in ξ from Eqn. 41 and doing a lot of expanding and neglecting of higher order terms, we arrive at

$$\kappa = - \frac{1}{R} - \left(\frac{n^2 - 1}{R^2} \right) \hat{\xi} e^{\sigma t} e^{in\theta} . \quad (50)$$

Then Eqn. 6 becomes

$$\Delta p|_{r=\xi} = \left[p - p_a \right]_{r=\xi} = \left[p^{(0)} + p^{(1)} - p_a \right]_{r=\xi} = \gamma \kappa \quad (51)$$

$$\left[p_a - \frac{\gamma}{R} - 12 \left(\frac{\mu v R}{b^2} \right) \log \left(\frac{r}{R} \right) + 12 \left[\frac{\mu R}{n b^2} \right] \left(\sigma + \frac{v}{R} \right) \hat{\xi} e^{\sigma t} \left(\frac{R}{r} \right)^n e^{i n \theta} - p_a \right]_{r=\xi} = \gamma \kappa \quad (52)$$

$$-12 \left(\frac{\mu v R}{b^2} \right) \log \left(1 + \left(\frac{\hat{\xi}}{R} \right) e^{\sigma t} e^{i n \theta} \right) + 12 \left(\sigma + \frac{v}{R} \right) \left(\frac{\mu R}{n b^2} \right) R^n \hat{\xi} \left(R + \hat{\xi} e^{\sigma t} e^{i n \theta} \right)^{-n} = -\gamma \left(\frac{n^2 - 1}{R^2} \right) \hat{\xi} e^{\sigma t} e^{i n \theta} \quad (53)$$

$$-12 \left(\frac{\mu v R}{b^2} \right) \left(\left(\frac{\hat{\xi}}{R} \right) e^{\sigma t} e^{i n \theta} \right) + 12 \left(\sigma + \frac{v}{R} \right) \left(\frac{\mu R}{n b^2} \right) \hat{\xi} e^{\sigma t} e^{i n \theta} = -\gamma \left(\frac{n^2 - 1}{R^2} \right) \hat{\xi} e^{\sigma t} e^{i n \theta} \quad (54)$$

$$-12 \left(\frac{\mu v}{b^2} \right) + 12 \left(\sigma + \frac{v}{R} \right) \left(\frac{\mu R}{n b^2} \right) = -\gamma \left(\frac{n^2 - 1}{R^2} \right), \quad (55)$$

which finally reduces to the dispersion relation for discrete modes $n = 2, 3, 4 \dots$

$$\sigma(n) = (n - 1) \left(\frac{v}{R} \right) - n(n^2 - 1) \left[\frac{\gamma b^2}{12 \mu R^3} \right]. \quad (56)$$

or, in dimensionless form,

$$(\sigma b/v) = (n - 1) \left(\frac{b}{R} \right) - n(n^2 - 1) \left[\frac{1}{12 \text{Ca}} \right] \left(\frac{b}{R} \right)^3, \quad (57)$$

which should be compared to the same result for continuous case, Eqn. 31. The dimensionless quantity (b/R) plays the role of the dimensionless wavenumber kb in the discrete case because if n oscillations of wavelength λ fit around a circular bubble of radius R , we have $n\lambda = 2\pi R = n(2\pi/k)$ so that $k = n/R$ and $kb = n(b/R)$. If we call $(kb)_n = n(b/R)$ a sort of discrete wavenumber, then Eqn. 57 becomes

$$(\sigma b/v)_n = \left(\frac{n - 1}{n} \right) (kb)_n - \left(\frac{n^2 - 1}{n^2} \right) \left[\frac{1}{12 \text{Ca}} \right] (kb)_n^3, \quad (58)$$

which is essentially identical to Eqn. 31, for larger values of n , but now with discrete allowed wavenumbers. To illustrate this, let us choose $b/R = 0.15$ and a range of values of Ca . Fig. 6 shows the results.

We can find the mode number with maximum growth rate n_{\max} by setting $d\sigma/dn = 0$. Some work leads to

$$n_{\max} = \mathbf{int} \left[\frac{1}{3} + 4 \text{Ca} \left(\frac{R}{b} \right)^2 \right]^{1/2}, \quad (59)$$

in which we understand \mathbf{int} to mean the *nearest integer*.

Just as in the continuous case, there is a largest mode number n_o such that all modes between $n = 2$ and $n = n_o$ have zero or positive growth rates, while all $n > n_o$ decay. We can find n_o by setting $\sigma b/v = 0$ in Eqn. 57 and solving for n . We find

$$n_o = \mathbf{int} \left[\left(12 \text{Ca} \left(\frac{R}{b} \right)^2 + \frac{1}{4} \right)^{1/2} - \frac{1}{2} \right], \quad (60)$$

in which \mathbf{int} means *the next smallest integer*. It is evident from Eqn. 60 that the range of unstable mode numbers increases with R/b . In particular, there is a series of threshold radii $R = R_{n_o}$ such

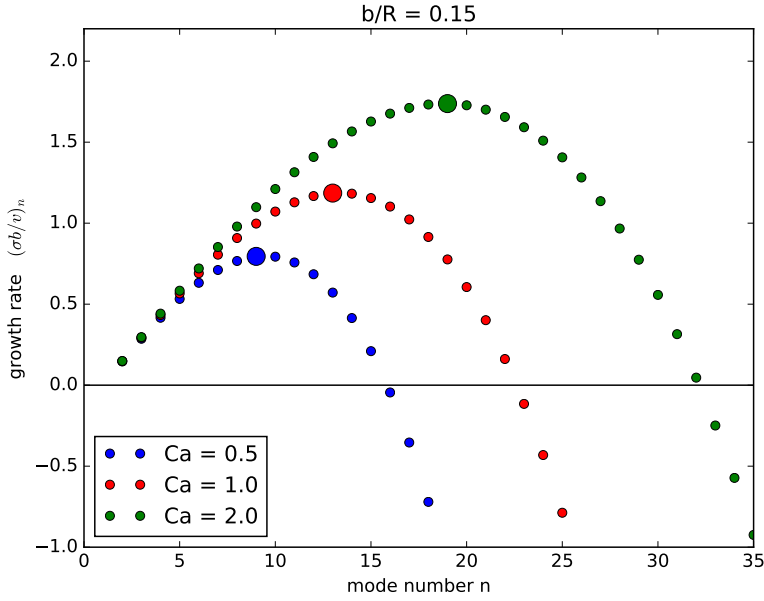


Figure 6: The dimensionless discrete dispersion relation $(\sigma b/v)$ vs. mode number n , for $b/R = 0.15$ and various values of $Ca = \mu v/\gamma$. Ca is effectively the dimensionless interface velocity. The larger symbols show the modes with the largest growth rates, which occur at $n = 9, 13, 18$ for $Ca = 0.5, 1.0, 2.0$.

that $n = (2, 3, 4 \dots n_o)$ are all unstable. In dimensionless terms, $(R/b)_{n_o}$ is given by inverting Eqn. 60 to get

$$(R/b)_{n_o} = \left[\frac{n_o(n_o + 1)}{12 Ca} \right]^{1/2}. \quad (61)$$

This means that really tiny bubbles with $R < R_2$ are completely stable, while bubbles with radii $R_2 < R < R_3$ are unstable with $n = 2$ and so on. Large bubbles are unstable to a wide, but still finite, range of $2 < n < n_o$. As a circular bubble grows, it passes through a cascade of radii R_{n_o} and more and more modes acquire positive growth rates and join the race to make fingers. At each stage, the fastest growing perturbations are the ones near $n = n_{\max}$, which also increases with the radius according to Eqn. 59.

C.3 beyond the 2D model: incorporating new effects

Real Hele-Shaw cells live in 3D. They are, at best, quasi-2D. The simple formulation of the previous sections, which dominates the early literature of the field [4, 5, 6, 7, 14], turns out to omit some important 3D details. The interface is actually a surface with *two* radii of curvature. If we assume that the oil completely wets the plates, then the shape of the interface in the direction perpendicular to the plates is a semicircle with a radius $b/2$. This curvature, plus some other subtle effects discussed below, are incorporated into a more realistic formulation [13, 16, 17] of the pressure jump boundary condition given by [17]

$$\Delta p = \left(\frac{\pi}{4} \right) \gamma \kappa + \frac{2\gamma}{b} \left(1 + JCa^{2/3} \right) - 2\mu \frac{\partial u}{\partial r} \Big|_{r=\xi}. \quad (62)$$

The first term is the same as Eqn. 6 except for a strange factor of $\pi/4$. This arises from a rigorous z -averaging of the in-plane curvature [16]. In the literature, the $\pi/4$ factor is often annoyingly absorbed into the surface tension parameter γ . The second $2\gamma/b$ term is the additional pressure jump due to the second radius of curvature $2/b$ in the z direction. It has no dynamical effect since it just shifts p_a by a constant amount.

The third term in Eqn. 62 involving $\text{Ca}^{2/3}$ is a dynamic correction to the pressure due to a moving interface. In effect, Eqn. 6 implicitly assumed a static bubble, which is equivalent to the limit $\text{Ca} \rightarrow 0$. The $\text{Ca}^{2/3}$ correction is just the first nontrivial term in an asymptotic expansion in powers of $\text{Ca}^{1/3}$ [16]. The dimensionless factor $J = 3.80$ was calculated numerically by Park and Homsy [16]. The advancing bubble also leaves behind a film of oil on the upper and lower plates, so this is often called the *dynamic wetting* term. The thickness of this film scales like $b\text{Ca}^{2/3}$ for small Ca and it can become quite substantial [13, 16, 21]. Indeed, you may observe the film slowly dripping from the top plate under gravity to form bridging islands of oil after the bubble has formed.

The final new term in Eqn. 62 is perhaps the most surprising. Known as the *viscous normal stress* term, it has nothing to do with the surface tension. It comes from properly balancing forces (*via* various terms in the viscous stress tensor) across the interface. Remarkably, its crucial significance in this problem was not appreciated until it was pointed out by Kim *et al* [20] in 2009, a bit more than 50 years after Saffman and Taylor's original paper [6].

When all these new effects are included, the dispersion relation $(\sigma b/v)_n$ is considerably more complex. In our notation, it is given by [17]

$$(\sigma b/v)_n = \frac{1}{S+W} \left\{ \left[n \left(1 + \frac{\delta}{3} \left(\frac{b}{R} \right)^2 \right) - S \right] \left(\frac{b}{R} \right) - n(n^2 - 1) \frac{(\pi/4)}{12 \text{Ca}} \left(\frac{b}{R} \right)^3 \right\} \quad (63)$$

$$S = 1 + \frac{\delta}{6} \left(\frac{b}{R} \right)^2 n(n+1) \quad (64)$$

$$W = \frac{nJ}{9 \text{Ca}^{1/3}} \left(\frac{b}{R} \right), \quad (65)$$

where $\delta = 1$ and $J = 3.80$ corresponds to including both wetting and viscous normal stress effects. Setting $\delta = 0$ turns off viscous normal stress and setting $J = 0$ turns off wetting. In that case, Eqn. 63 reduces to Eqn. 57 (except for the pesky factor of $\pi/4$). Fig. 7 compares the various models. The new dispersion curve has the same general features as the simple model, but analytic expressions for n_{\max} , n_o , and $(R/b)_{n_o}$ are cumbersome.

Maxworthy [18] showed experimentally that the traditional 2D theory, plus various extensions of it to include wetting, greatly overestimated the number of fingers for $\text{Ca} > 10^{-2}$ or so. This more physically complete theory brings better [17], although perhaps still not perfect [21], agreement with experiments up to $\text{Ca} \sim 1$.

C.4 some loose ends

In the above calculations, we have treated the radial speed v and the gas pressure in the bubble p_a as if they were independent parameters. But in fact, the size of p_a controls v . In the experiment, what is measured by the pressure gauge is **not** p_a itself, but rather the so-called *gauge pressure* $p_g = p_a - p_{\text{atm}}$, the difference between the bubble pressure and the atmospheric pressure of the air in the room. What drives the radial flow is really p_g , since the oil returns to atmospheric pressure

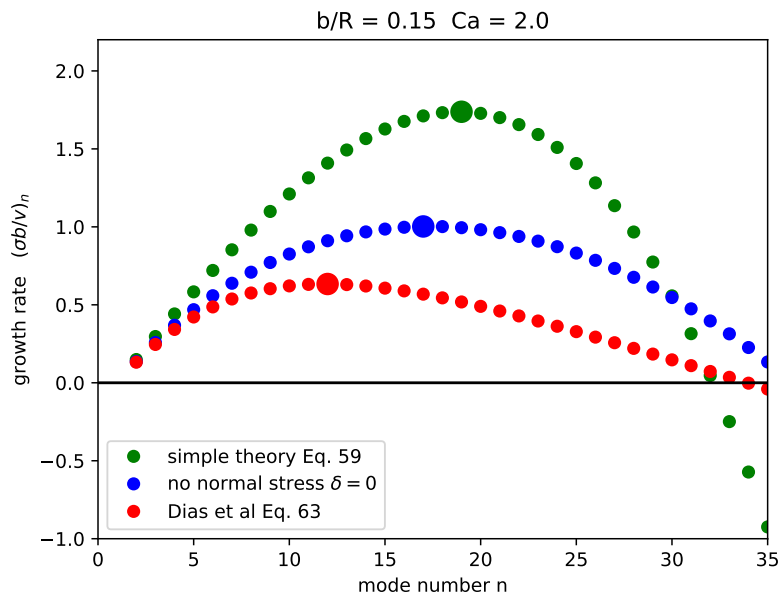


Figure 7: The dimensionless dispersion relation $(\sigma b/v)$ vs. mode number n , for $b/R = 0.15$ and $Ca = \mu v/\gamma = 2.0$. For the simple model (in green, same as the green points in Fig. 6), with wetting effects, but no viscous normal stress (blue points, $\delta = 0$) and for the full model of Dias *et al* [17] (red points). The larger symbols show the modes with the largest growth rates, which occur at $n = 19$ for the simple model and $n = 12$ for the full model.

when it gets to the edge of the round top plate of the Hele-Shaw cell. The speed v depends on the viscous resistance of the oil between the radius of the bubble (or the tip of a finger) and the outer radius of the cell. This is obviously pretty complicated for a fractal bubble, especially when a finger approaches the outer radius. You may observe the sudden acceleration of such fingers as they quickly form leak paths that ultimately let the air out of the bubble.

In practice, we just use the measured p_g and the setting of the needle valve as proxies for controlling v and then directly measure R and v from the images. The velocity v only enters the problem *via* the dimensionless capillary number Ca . The bubble pressure p_a does not enter into the stability at all, except indirectly. In fact, most theoretical work only considers the case of constant v (and hence constant Ca), rather than the case of constant pressure, in which v varies. But constant pressure is much easier to realize experimentally if the injected fluid is a gas.

C.5 applying linear stability theory

We can use linear stability theory to predict the number of fingers we observe, as long as we remain in the regime where the theory is valid — the limit of small, non-interacting fingers. This “linear regime” is not sharply defined (the linear theory is only strictly mathematically valid for *infinitesimal* fingers), but may reasonably be taken to be the early stages of finger growth, before obvious interactions, such as shadowing, are observed. The data analysis code `mean_radius.py` calculates the mean radius of the bubble, as well as the standard deviation and maximum and minimum radii, as the bubble grows. The standard deviation remains small until the fingers appear, so you can use the point at which it begins to increase sharply as indicating the end of the linear

regime. You can also simply scrutinize the images and choose the latest one for which the fingers are still small but easily counted [18].

To use the linear stability theory, we need to deal with the fact that the growth rate σ_n depends on R and v , but these quantities are continuously changing with time as the bubble grows. One simple idea that is commonly used [18] is to use the mode n_{\max} for which σ_n is maximum for the *initial* values R_0 and v_0 , just as the bubble begins its expansion. This makes some sense because the modes that get started first have a head start and are likely to grow the largest. They might even suppress nearby modes *via* nonlinear shadowing.

To make a more detailed theory which accounts for the modes that join the race later, we must calculate not $e^{\sigma_n t}$ for each n , but an integral [4, 17]

$$\xi_n(t) = \xi(0) e^{I_n(t)} \quad \text{with} \quad I_n(t) = \int_0^t \sigma_n(t') dt' , \quad (66)$$

where $\sigma_n(t)$ comes from Eqn. 63, using the measured $R(t)$ and $v(t)$. Here $\xi(0)$ is the magnitude of the initial noise in the experiment, assumed to be the same for all modes. In the integral, we only include contributions for which $\sigma_n(t) \geq 0$, so that the “noise floor” remains $\xi(0)$ for all modes for all time. Thus, modes may grow later on as the bubble grows, but once started, no mode decays. Obviously, this scheme entails some assumptions about the distribution of noise in the experiment.

To predict the number of fingers, we calculate the relative growth of the various n and choose the number with the largest accumulated relative growth $\xi_n(t)/\xi(0)$. A numerical scheme is implemented in the python code `linear_theory.py` to do this from data.